Influence of passivating interlayers on the carrier selectivity of MoOx contacts for c-Si solar cells

Ah Sen, M.T.S.K.; Janssen, Gaby; Mewe, Agnes; Bronsveld, Paula ; Melskens, Jimmy; Hashemi, Fatemeh; Procel Moya, P.A.; Weeber, A.W.

DOI
10.1051/epjpv/2024030

Publication date
2024

Document Version
Final published version

Published in
EPJ Photovoltaics

EPJ Photovoltaics **15**, 34 (2024)

https://doi.org/10.1051/epjpv/2024030

Available online at:
www.epj-pv.org

ORIGINAL ARTICLE OPEN ACCESS

Influence of passivating interlayers on the carrier selectivity of MoO_x contacts for c-Si solar cells

Mike Tang Soo Kiong Ah Sen[1,2,*], Gaby Janssen[1], Agnes Mewe[1], Paula Bronsveld[1], Jimmy Melskens[1,3], Fatemeh Hashemi[1], Paul Procel-Moya[2], and Arthur Weeber[1,2]

[1] TNO Energy Transition Solar Energy, P.O. Box 15, NL-1755 ZG Petten, The Netherlands
[2] Delft University of Technology, PVMD group, Mekelweg 4, NL-2628 CD Delft, The Netherlands
[3] AIKO Energy Netherlands B.V. (Eironn Netherlands B.V.), Schiphol Boulevard 201, Tower D6, 1118 BG Schiphol, The Netherlands

Received: 20 February 2024 / Accepted: 4 September 2024

Abstract. The application of molybdenum oxide (MoO_x) as a hole-selective contact for silicon-based solar cells has been explored due to superior optical transmittance and potentially leaner manufacturing compared to fully amorphous silicon-based heterojunction (SHJ) devices. However, the development of MoO_x contacts has been hampered by their poor thermal stability, resulting in a carrier selectivity loss and an S-shaped IV curve. The aim of this study is to understand the influence of different passivating interlayers on the carrier selectivity of hole-selective MoO_x contacts for crystalline silicon (c-Si) solar cells. We highlight the effect of different interlayers on the surface passivation quality, contact selectivity, and the thermal stability of our MoO_x-contacted devices. The interlayers studied are intrinsic hydrogenated amorphous silicon (a-Si:H(i)), thermally grown ultrathin SiO_2, and a stack consisting of an ultrathin SiO_y and Al_2O_3 layer. Additionally, we simulate the interacting interlayer properties on the carrier selectivity of our MoO_x contacts using a simplified model. Among these interlayers, the Al_2O_3/SiO_y stack shows to be a promising alternative to SiO_2 by enabling efficient transport of holes while being able to sustain an annealing temperature of at least 250 °C underlining its potential in module manufacturing and outdoor operation.

Keywords: MoO_x hole-selective contact / surface passivation / passivating interlayers / metal oxide / c-Si solar cells

1 Introduction

Currently, the conversion efficiencies of conventional homojunction crystalline silicon (c-Si) solar cells are mainly limited by the recombination of charge carriers occurring at the metal/silicon interface. This limitation is minimized by including a stack of passivating and carrier-selective layers in between the Si absorber and metal electrodes which effectively suppresses the recombination at the c-Si surface while simultaneously being conductive to either electrons or holes generated in the c-Si absorber. Nowadays, the highest conversion efficiency of Si solar cells comprising amorphous silicon heterojunction (SHJ) or doped polycrystalline Si contacts are manufactured by using this type of so-called passivating contact scheme [1,2]. Nevertheless, these highly doped Si-based passivating contacts are a source of parasitic absorption, which consequently reduces the total amount of photogenerated carriers inside the Si absorber, resulting in a lower current. For instance, doped poly-Si, typically used in passivating contact structures, suffers from high parasitic absorption when heavily doped [3]. In the case of amorphous silicon, its direct band gap of approximately 1.7 eV in combination with its heavily doped layers hinder the short-circuit current density (J_{sc}) of SHJ solar cells [4,5].

In order to minimize the J_{sc} losses sustained by these layers, alternative transparent selective contacts, such as metal oxides have been explored due to their wide bandgap, capability to extract charge carriers, passivation quality on c-Si, and the relatively simple physical vapor deposition (PVD) techniques that have been used to fabricate them [6,7]. For instance, evaporated MoO_x has been investigated for its transparency in the blue wavelength region and its ability to act as a hole-selective contact for c-Si solar cells [8–11]. Recently, a conversion efficiency of 23.83% has been achieved by replacing the p-type hydrogenated amorphous silicon (a-Si:H(p^+)) layer with a MoO_x hole-selective

* e-mail: m.t.s.k.ahsen@tudelft.nl

contact in a SHJ solar cell structure [12]. Nevertheless, a MoO_x/a-Si:H(i)/c-Si contact has been shown to degrade considerably at standard SHJ annealing conditions [13,14], causing the appearance of an S-shaped current–voltage (IV) curve, and accordingly a loss in fill factor (FF). Additionally, while the doped a-Si:H layer is omitted in that structure, the intrinsic a-Si:H layer is still used, meaning that the high transparency of the MoO_x layer is not fully exploited due to the absorptive nature of the intrinsic a-Si:H (a-Si:H(i)) layer. The lack of thermal stability of the MoO_x/a-Si:H(i)/c-Si contact is a significant limitation in the potential manufacturing of the SHJ-like solar cell, since an annealing temperature of about 200 °C is often required to recover from sputtering damage after deposition of the transparent conductive oxide (TCO) layer and is an essential back-end treatment during metallization and TCO post-crystallization. While a MoO_x/a-Si:H(i)/c-Si contact provides excellent surface passivation properties, the insertion of an a-Si:H(i) interlayer poses several transport issues which could result in the formation of the S-shaped IV curve.

In search of alternative passivating interlayers, ultrathin SiO_2 layers (<2 nm) are a potential candidate in replacing a-Si:H(i) due to their ability to provide excellent surface passivation and contact selectivity when combined with doped poly-Si contacts [15]. However, unlike poly-Si contacts where excellent passivation properties can be achieved, the insertion of an oxide interlayer results in apparent hole collection issues when combined with MoO_x even though sufficient band bending is typically obtained at the c-Si interface [16–19]. Conversely, the selectivity of MoO_x contacts with an Al_2O_3 interlayer has shown to be promising with good surface passivation and contact resistance properties [20]. In addition, we recently showed that an ultrathin atomic layer deposited (ALD) Al_2O_3/SiO_y interlayer stack does not impede the hole selectivity provided by the MoO_x contact, resulting in good contact selectivity and cell performance [21]. Note that the ultrathin SiO_y is naturally formed at the c-Si surface during the initial cycles of the ALD Al_2O_3 process, as has been repeatedly documented elsewhere [22,23].

The aim of this work is to further understand the interaction between the salient factors of the passivating interlayer, or interlayer stack, and MoO_x contact that influence contact selectivity. A comparative study between different interlayers, notably a-Si:H(i), SiO_2, and Al_2O_3/SiO_y is made where the non-ideal carrier extraction behavior, caused by the insertion of an interlayer on our MoO_x-based contact, is addressed. Since the carrier transport mechanisms of the aforementioned contacts involve different transport mechanisms, such as band-to-band tunneling, defect-assisted transport, thermionic emission, and pinhole aided transport, a simple model is developed to encompass the different transport properties of these interlayers. In this model, the carrier transport through the interlayer is represented by a thin layer with limited effective charge carrier mobility. This simplified approach facilitates a meaningful comparative interpretation of the impact on majority carrier transport across the interlayers in relation to the observed loss in carrier selectivity.

2 Methodology

2.1 Solar cells fabrication and characterization

To investigate the impact of the different interlayers on the solar cell performance, n-type c-Si solar cells with MoO_x-based contacts at the front are studied. A rear poly-Si(n^+) contact is used because of its excellent surface passivation quality, contact resistance, and thermal stability, such that the front MoO_x-based contact is limiting in the measurements and not the rear poly-Si contact.

The manufacturing steps of the solar cells with front side thermal SiO_2, Al_2O_3/SiO_y or a-Si:H(i) interlayers and the cell schematic are shown in Figure 1. The 6-inch, 180 µm-thick pseudo-square Cz c-Si(n) substrates with a resistivity of about 3 Ω cm were processed as follows: textured in a KOH solution, pre-gettered with $POCl_3$ diffusion followed by phosphosilicate removal, surface smoothing etch, and finally cleaned in RCA 1 and 2, and nitric acid oxidation step (NAOS) solutions. Note that the surface smoothing is only a minor surface treatment in the sense that the textured morphology is still preserved overall. The substrates were dipped in a 1% HF solution prior to the formation of the rear SiO_2/poly-Si(n^+) contact. The SiO_2 interlayer (∼1.3 nm) was thermally grown in a low pressure chemical vapor deposition (LPCVD) chamber at 610 °C using an O_2 and N_2 mixture. Subsequently, the poly-Si(n^+) layer was formed through a two-step process: initial deposition of a 20 nm thick a-Si:H (n^+) layer using plasma-enhanced chemical vapor deposition (PECVD), followed by a 20 minute thermal annealing in N_2 at 900 °C to induce crystallization. After this poly-Si (n^+) formation process, the contact was subjected to a hydrogenation process using PECVD with NH_3 plasma at 375 °C to reduce interface defects and improve passivation. In the case of an ultrathin SiO_2 interlayer, the thermal oxide at the front side was preserved. The samples with a-Si:H(i) and Al_2O_3/SiO_y interlayers were dipped in a 1% HF bath to remove the front thermal oxide. Subsequently, the a-Si:H(i) and Al_2O_3/SiO_y interlayers were deposited using PECVD and spatial ALD tools, respectively. 8 cycles of spatial ALD Al_2O_3 were used to deposit a 1.5 nm thick Al_2O_3/SiO_y stack. These layers were deposited using a Levitrack deposition tool without any subsequent post-deposition annealing treatment. The samples without interlayer only received an HF dip prior to MoO_x deposition. Next, the samples were transferred to an electron beam physical vapor deposition (PVD) tool where a 5 nm MoOx layer was deposited in a high vacuum (7×10^{-6} mbar) environment. Note that minimal X-ray damage to the surface passivation of the MoO_x contacts was observed after the electron beam deposition, likely due to the low deposition power used, as shown in Appendix A. Finally, indium tin oxide (ITO) films were deposited in a sputtering tool on both sides of the samples and a full area Ag sheet was also deposited at the rear side by sputtering. To finalize the solar cells, a front Ag grid was screen printed using a low temperature Ag paste and the device was cured in air at different temperatures (190–250 °C).

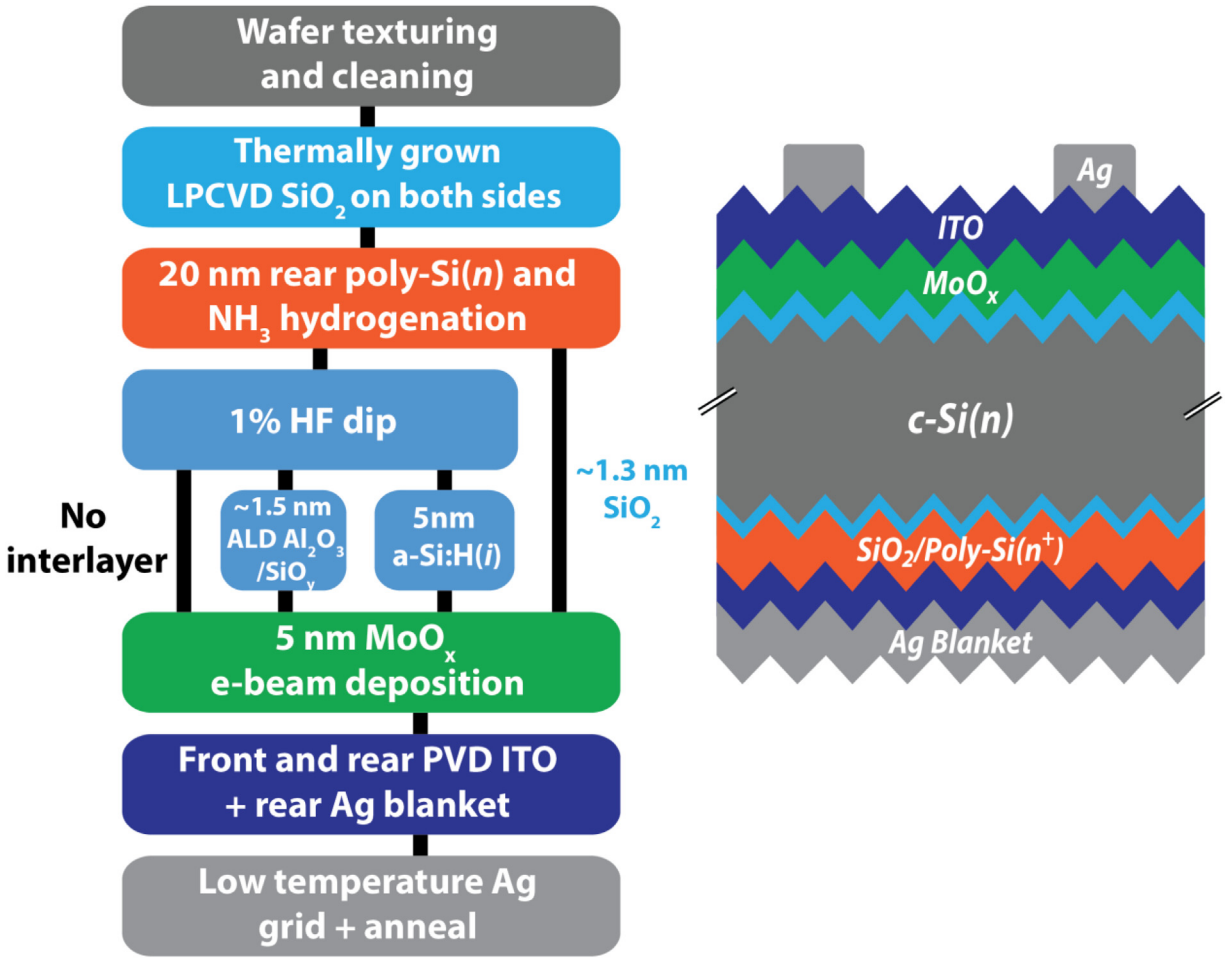

Fig. 1. Process flow for the manufacturing of the solar cells with different interlayers (left) and a schematic of the solar cells (right).

The photoconductance of charge carrier lifetime samples was measured by using a Sinton WCT-120 system, as well as the internal voltage expressed in terms of the implied open circuit voltage iV_{oc}. The external V_{oc} of the half-fabricated cells were measured by a *Suns* V_{oc} Sinton tool which does not require metal contacts due to the conductivity of the ITO films, as shown in Figure 2. The solar cells were characterized by *IV* measurements in a Wacom AAA solar simulator at standard test conditions. The results were corrected for spectral mismatch. Dark *IV* measurements were performed at varying temperatures between 25 and 65 °C using the Wacom solar simulator. The interlayer films were deposited on single-side polished c-Si wafers with unpolished backsides to eliminate back reflections during ellipsometry measurement. The thickness of the interlayers was determined using a spectroscopic ellipsometer (J.A. Woollam Co., Inc.). Ellipsometric data was collected at three angles of incidence (60°, 70°, and 80°) and over a photon energy range of 1.1 to 5 eV. The Cauchy model was used to analyze oxide layers.

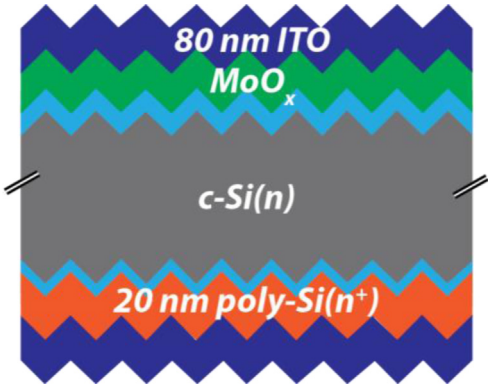

Fig. 2. Solar cell precursors with front MoO_x and rear poly-Si (n^+) contacts for iV_{oc} and *Suns* V_{oc} measurements.

2.2 Simulations and calculations

2D simulations were performed by using the Atlas package of Silvaco [24]. Figure 3 depicts the cell structure used in the simulations. The front contact consists of an ultrathin interlayer with limited carrier mobility, hole-selective layer with a varying work function (*WF*), and a metal electrode. The rear electron contact is built similarly to the hole contact but consists of optimized parameters that minimize the recombination and contact resistivity.

This model intends to simulate the effects of the surface passivating interlayers and MoO_x layer on the carrier selectivity of the hole contact. Therefore, for the sake of simplicity, we mimic the effect of MoO_x by using the

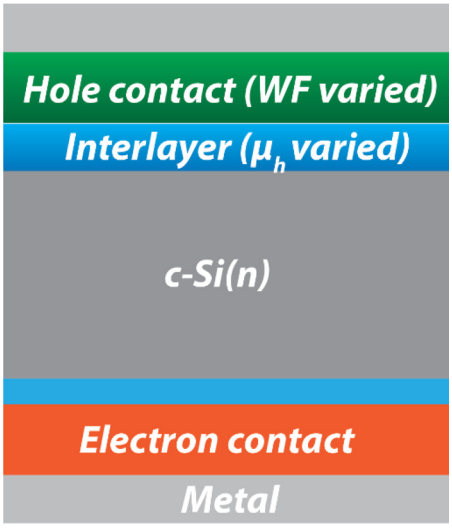

Fig. 3. Schematic of the cell structure used in Atlas to simulate the contact selectivity of the cell with varying interlayer μ_h and hole *WF*.

properties of a *p*-type material based on a poly-silicon contact as shown in [25]. In this regard, the transport of holes is simplified at the hole contact and metal electrode. This assumption is only valid for comparison purposes as we focus on the study of interlayer with different *WF* for the hole contact layer. In this simplification, the variation in the *WF* of this contact is represented by changing the doping level of the *p*-type poly-Si hole contact. We assume the carrier mobility in the interlayer as the parameter affecting the selectivity of the hole contact [26,27]; the hole mobility (μ_h) value characterizes the actual physical mechanism of the charge transport across the interlayer [25]. This simplified approach facilitates a meaningful comparative interpretation of the impact on majority carrier transport across the interlayers in relation to the observed loss in carrier selectivity, while avoiding unnecessary complexity introduced by incorporating different possible transport mechanisms throughout the interlayers.

Accordingly, in this study, simulations with different mobility values emulate the behavior of the device using different interlayer materials. Table 1 shows the values of the simulation parameters for the c-Si(n) absorber as well as the hole and electron contacts. The interlayer is modelled as a 1.5 nm c-Si(i) thick layer where μ_h is varied. Mobility values are varied between 10^{-2} and 10^{-7} $cm^2\,V^{-1}\,s^{-1}$ in this simulation work. Mobility values around 10^{-2} $cm^2 \cdot V^{-1} \cdot s^{-1}$ are indicative of an interlayer with minimal transport resistance. Conversely, an exceedingly low value of 10^{-1} $cm^2 \cdot V^{-1} \cdot s^{-1}$ or lower corresponds to resistances calculated for the quantum tunnelling of holes through an ideal, defect-free SiO_2 interlayer [25,28]. The electron mobility of the interlayer is set at 10^{-5} $cm^2 \cdot V^{-1} \cdot s^{-1}$ which represents electron carrier mobility for a tunneling SiO_2 and a-Si:H(i) interlayers. The effective surface recombination velocity (S_{eff}) of the hole contact is a crucial parameter in our simulation model, as it directly influences the recombination losses at the interface. In our analysis, the S_{eff} value is systematically varied over a wide range, from 10 cm/s (representing a nearly ideal passivated surface) to 10^5 cm/s (indicating a highly defective interface). By simulating the device performance across this range, we can assess the sensitivity of ΔV_{oc} and *FF* to variations in S_{eff}, and therefore quantify the impact of the hole contact quality on overall the solar cell efficiency.

3 Results

3.1 Interlayer surface passivating properties of MoO_x contacts

In this section, we investigate and compare the influence of different interlayers, i.e. a-Si:H(i), ultrathin spatial ALD Al_2O_3/SiO_y, and thermally grown SiO_2, on the surface passivation provided by the contact structures. The thickness of the thermal oxide − measured by ellipsometry − is around 1.3 nm and the oxide layer is combined with our poly-Si contacts. In comparison, the combined thickness of the Al_2O_3/SiO_y stack is around 1.5 nm after 8 spatial ALD cycles to grow Al_2O_3. To analyze the surface passivation properties of the interlayers on our MoO_x contacts, the iV_{oc} value is monitored after the deposition of MoO_x and ITO layers, and a subsequent annealing at 190 °C, as shown in Figure 4. The distribution of iV_{oc} values for each group, represented by box and whisker plots, is based on measurements from five samples per group. The MoO_x contact without an interlayer shows poor surface passivation, which can be mainly attributed to the poor surface passivation properties of the sub-stoichiometric oxide formed during the initial growth of the evaporated MoO_x layer [31]. However, the surface passivation of our MoO_x contacts improves by introducing the thermally grown SiO_2 and ALD grown Al_2O_3/SiO_y interlayers. On the other hand, excellent surface passivation is achieved by using an a-Si:H(i) interlayer. iV_{oc} above 700 mV is achieved after an annealing treatment at 190 °C. Subsequently, ITO layers were sputtered on the front and rear contacts. Interestingly, iV_{oc} improves for cell precursors with an Al_2O_3/SiO_y interlayer and without interlayer. In contrast, iV_{oc} decreases for precursors with SiO_2 and a-Si:H(i) interlayers due to the sputtering damage originated from the ITO deposition [32,33]. However, the sputtering damage can be partially recovered after an annealing treatment. Samples with an Al_2O_3/SiO_y interlayer and with no interlayer show no change in iV_{oc} after annealing at 190 °C.

3.2 Effect of interlayer properties on the contact selectivity of MoO_x contacts

To investigate the contact selectivity of our MoO_x contacts, we use the difference in internal and external V_{oc} ($\Delta V_{oc} = iV_{oc}\text{-}V_{oc}$) as a simple figure of merit with low values signifying a high carrier selectivity [34]. In case of low contact selectivity, the external V_{oc} of the cell is much lower than the internal V_{oc}, resulting in a high ΔV_{oc} value. This implies that the transport of majority carriers to the electrode is hindered. Note that the cell precursor used to measure the iV_{oc} and V_{oc} is shown in Figure 2.

Table 1. Atlas simulation parameters for the different layers.

	Parameter	Value
c-Si(n) absorber	Thickness	180 µm
	Resistivity	5 Ω.cm
	μ_e and μ_h	Klaassen model [29]
	SRH lifetime	3 ms
	Fermi level	4.74 eV
	Intrinsic concentration	8.6×10^9 cm^{-3}
	Auger lifetime	Richter model [30]
n-contact	Doping level	3×10^{20} cm^{-3}
	μ_h and μ_e at interlayer	10^{-3} cm^{2}V^{-1}s^{-1}
	Interlayer thickness	1.5 nm
p-contact	μ_h and μ_e at interlayer	10^{-2}– 10^{-7} cm^{2}V^{-1}s^{-1}
	Work function	4.91 − 5.33 eV
	Interlayer thickness	1.5 nm
	S_{eff}	10 − 10^5 cm/s

Figure 5 shows ΔV_{oc} for different MoO_x contacts in their as-deposited states and as a function of annealing temperature. These samples were annealed in air at a starting temperature of 190 °C − which represents the standard SHJ annealing conditions − followed by cumulative annealing up to 250 °C, with a 20 °C temperature step. The insertion of a-Si:H(i) and Al_2O_3/SiO_y interlayers does not affect the ΔV_{oc} prior to annealing and results in comparable ΔV_{oc} to the MoO_x/c-Si contact. In the case of a thermal SiO_2 interlayer, a high ΔV_{oc} value of about 258 mV is observed prior to annealing and no major change in ΔV_{oc} is observed after subsequent annealing. For the MoO_x/a-Si:H(i) contact, a steady increase in ΔV_{oc} from 15 to 30 mV is measured upon an increase in thermal budget, consistent with previous literature [14,35]. This decrease in selectivity is attributed to a reduction in the induced band bending at the MoO_x contact. This reduction in band bending is likely due to a decrease in the MoO_x *WF*, potentially caused by hydrogen effusion from the a-Si:H(i) interlayer and/or the formation of a parasitic layer at the MoO_x/a-Si:H(i) interface [14,35]. In comparison, the contact selectivity of the $MoO_x/Al_2O_3/SiO_y$ contact improves upon annealing at 190 °C and remains stable after further increases in annealing temperature; an average ΔV_{oc} of about 5 mV is measured after an annealing treatment at 230 °C with a slight increase observed following annealing at 250 °C.

3.3 Effects of passivating interlayers on *IV* characteristics

In this section, we investigate the influence of the passivating interlayers on the light *IV* parameters. The light *IV* curve and characteristics of the solar cells are shown in Figure 6 and Table 2. As expected, a MoO_x/a-Si:H(i) contact results in a high V_{oc} due to the excellent surface passivation of the a-Si:H(i) interlayer, but is limited by the contact selectivity loss after annealing. On the other hand, while ultrathin Al_2O_3/SiO_y and SiO_2 interlayers have shown a similar surface passivation quality (as shown in Appendix B), the high carrier selectivity loss of the MoO_x/SiO_2 contact results in a lower V_{oc} and *FF* in comparison to the $MoO_x/Al_2O_3/SiO_y$ contact. Finally, solar cells with a-Si:H(i) and Al_2O_3/SiO_y interlayers at the hole contact result in comparable conversion efficiencies just above 18%; the J_{sc} and *FF* values are higher for the $MoO_x/Al_2O_3/SiO_y$ contact due to superior transparency and carrier selectivity, respectively.

3.4 Interlayer transport: temperature-dependent dark *IV*

Further insights to explain the difference in ΔV_{oc} associated with different oxide interlayers can be acquired by performing a temperature-dependent dark *IV* analysis. Series resistance (R_s) is extracted from the 2-diode model for temperatures in the 25–65 °C range for the SiO_2 and Al_2O_3/SiO_y interlayers, as shown in Figure 7. An indirect measurement of the band offsets between the c-Si and the interlayer can be made by extracting the activation energy E_a from the slope of the temperature-dependent series resistance R_s by assuming an Arrhenius dependency [36]. As a result, we obtain E_a values of 117 meV and 2390 meV for the $MoO_x/Al_2O_3/SiO_y$ and MoO_x/SiO_2 contacts, respectively. E_a of the Al_2O_3/SiO_y interlayer is considerably lower than the thermally grown oxide which indicates that an inefficient hole carrier transport exists for the thermally grown SiO_2 interlayer. To further determine the effect of hole majority transport on the carrier selectivity of the contact, we simulate the effect of the interlayer hole mobility and contact *WF* on the hole contact properties.

3.5 Simulation of MoO_x contacts

3.5.1 Effect of surface passivation on the carrier selectivity

In this section, the influence of the surface passivation and μ_h properties of the interlayers on the carrier selectivity are simulated with respect to varying hole contact *WF*. We

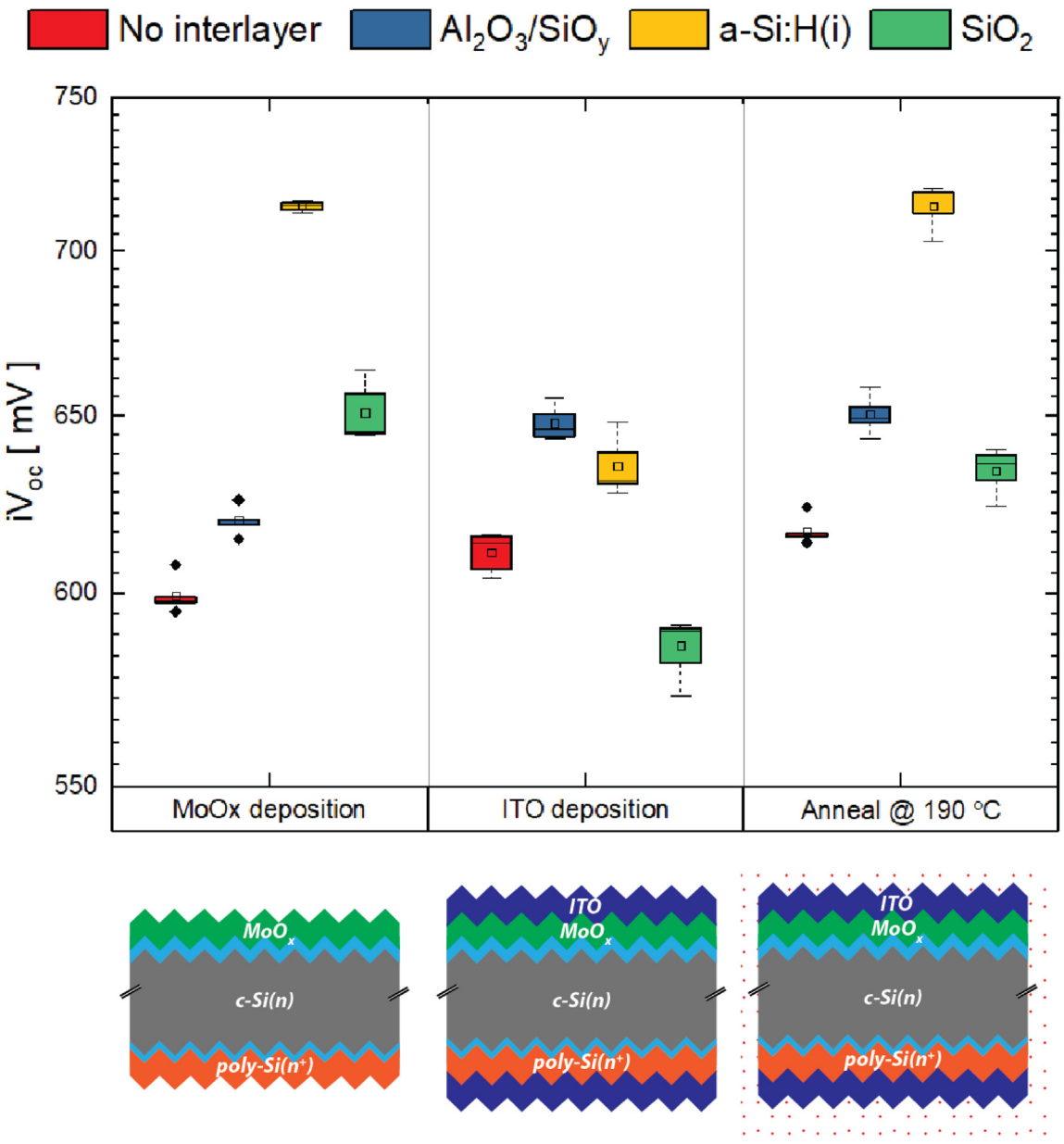

Fig. 4. iV_{oc} of half-fabricates after deposition of MoO_x and ITO layers and subsequent annealing at 190 °C. Note that the order of the interlayer configurations (no interlayer, Al_2O_3/SiO_y, a-Si:H(i), and SiO_2) is consistent across all figures.

first investigate the influence of the surface recombination properties of the interlayer on the hole selectivity. Figures 8a and 8b show the simulation results of the dependence of the hole selectivity on S_{eff}, contact WF, and μ_h. As expected, a lower hole contact WF leads to a loss in ΔV_{oc} due to a decreased hole concentration near the interface. The decrease in concentration elevates the hole resistance (R_h) across the contact, which is inversely proportional to the both carrier concentration and the hole mobility [26].

Additionally, S_{eff} of the interlayer has a significant influence on the ΔV_{oc} of the contact, particularly for interlayers with low mobility ($\mu_h = 10^{-7}$ cm^2 V^{-1} s^{-1}). Interestingly, an increase in ΔV_{oc} is observed with decreasing S_{eff}. This counterintuitive behavior can be explained by the competing contributions of hole resistance within the interlayer ($R_{h,int}$) and the absorber ($R_{h,abs}$), as highlighted by Onno et al. [37]. ΔV_{oc} depends on both components, and the relationship is described by:

$$\Delta V_{oc} = \left(J_{r,surf} + J_{r,m}\right)\cdot R_{h,abs} + J_{r,m}\cdot R_{h,int} \qquad (1)$$

where $J_{r,\,surf}$ and $J_{r,m}$ are recombination current density at the Si surface and metal contact, respectively. Consequently, for an interlayer with $\mu_h = 10^{-7}$ cm^2 V^{-1} s^{-1}, decreasing S_{eff} shifts the recombination dominance towards the surface, increasing $J_{r,surf}$ at the expense of $J_{r,m}$.

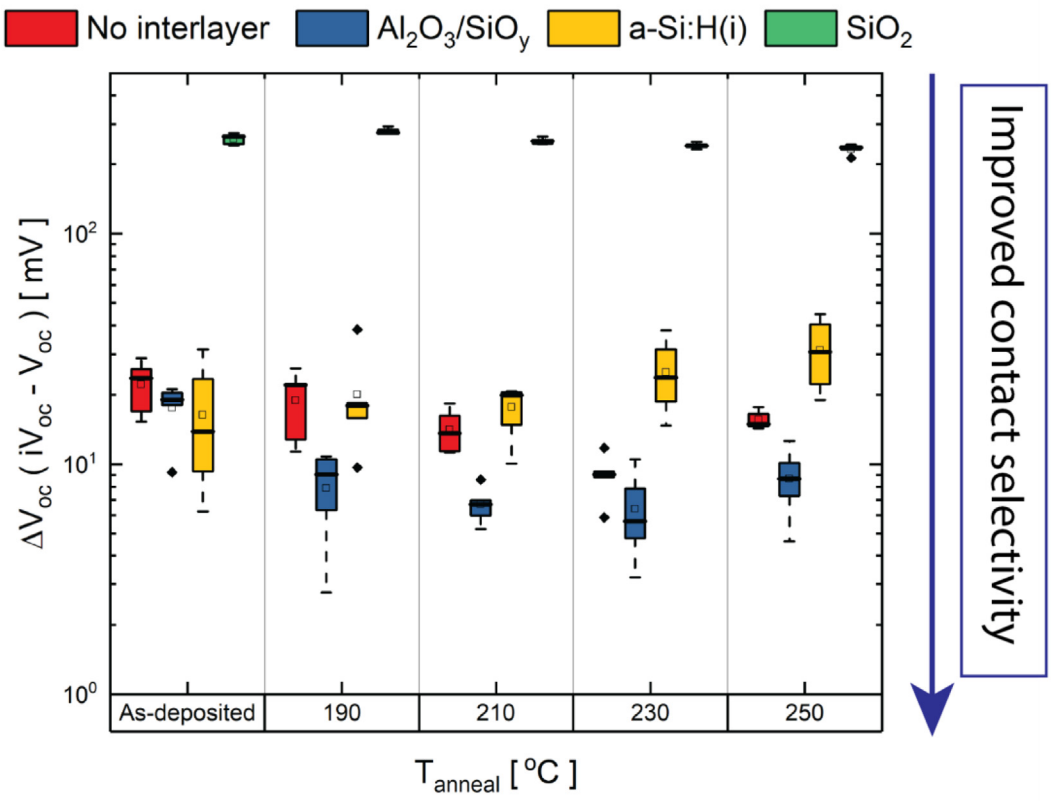

Fig. 5. ΔV_{oc} behavior of different MoO_x contacts as a function of cumulative annealing (190–250 °C).

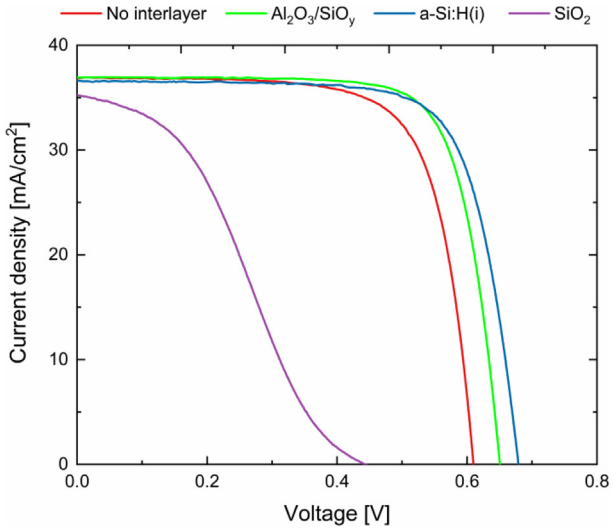

Fig. 6. Influence of passivating a-Si:H(i), Al_2O_3/SiO_y, and SiO_2 interlayers on the light IV characteristics of the solar cells with MoO_x contacts and different interlayers (right).

3.5.2 Effect of interlayer hole mobility on the carrier selectivity

Figures 9a and 9b show the simulated interacting effect of μ_h and contact WF on the cell ΔV_{oc} and FF, respectively. S_{eff} of the contact was set to 33 cm/s (as shown in Appendix B) which approximately represents the surface passivation of the MoO_x contacts with Al_2O_3/SiO_y and SiO_2 interlayers. At $WF > 5.25$ eV, ΔV_{oc} is minimal since the majority concentration is high enough which effectively reduces $R_{h,abs}$ (referring to Eq. (1)), even for a interlayer with low mobility ($\mu_h = 10^{-7}$ cm^2 V^{-1} s^{-1}). This reduction in $R_{h,abs}$ allows for efficient hole extraction, minimizing recombination losses and maintaining a high V_{oc}, even with less optimal interlayer transport properties. However, for this high WF, a steep decrease in FF is noted at $\mu_h = 10^{-7}$ cm^2 V^{-1} s^{-1}. At moderate WF (5.1–5.2 eV), noticeable selectivity and FF losses are observed with a strong dependence on μ_h; a decrease in μ_h of the interlayer yields higher ΔV_{oc} and FF losses. However, at $WF < 5.1$ eV, contact selectivity cannot be maintained anymore even for high μ_h of the interlayer. The simulation results indicate that for both the SiO_2 and Al_2O_3 interlayers the MoO_x WF in the range of 5.1–5.2 eV is found. This estimation is supported by the close agreement between the simulated ΔV_{oc} values and the experimental measurements presented in Figures 5a and 9a, respectively. The moderate WF range is defined as the values where a good selectivity can be achieved with sufficient hole mobility provided by the interlayer. The significantly high ΔV_{oc} and FF losses, measured for our MoO_x/SiO_2/c-Si(n) contact, suggest that the SiO_2 interlayer corresponds to a μ_h in the vicinity of 10^{-7} to 10^{-8} cm^2 V^{-1} s^{-1}. This observation is consistent

Table 2. Measured *IV* characteristics for solar cells with different interlayers and without an interlayer.

Passivating interlayer	J_{sc} [mA/cm^2]	V_{oc} [mV]	*FF* [%]	Efficiency [%]
No interlayer	36.9	610	72.1	16.2
Al_2O_3/SiO_y	36.9	651	75.6	18.2
a-Si:H(i)	36.2	679	73.8	18.1
SiO_2	35.2	440	34.6	5.4

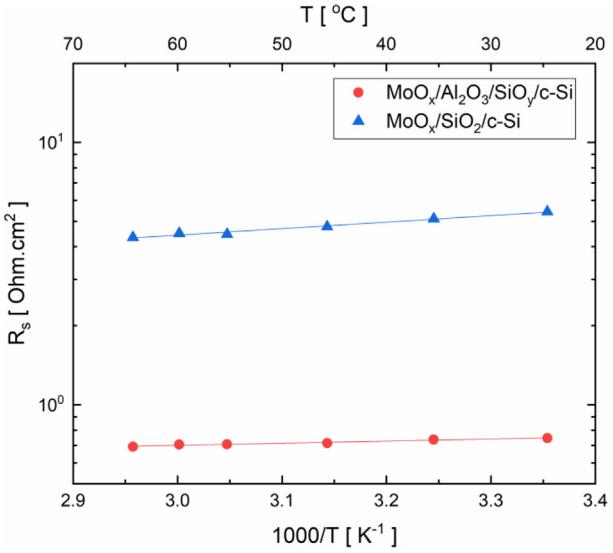

Fig. 7. Dark *JV* measurements were used to extract R_s as a function of cell temperature (25–65 °C). The fitted lines are used to calculate the activation energy.

with the characteristics of the thermal SiO_2 interlayer and supports the proposed mobility for a defect-free SiO_2 interlayer, with a thickness ranging from 1.1 to 1.5 nm [25]. On the other hand, the evident reduction in both ΔV_{oc} and *FF* within our MoO_x/a-Si:H(i)/c-Si(n) contact, as influenced by an elevated thermal budget treatment, exhibits a good correlation with an interlayer mobility of about 10^{-5} cm^2 V^{-1} s^{-1} or slightly higher. Finally, the good ΔV_{oc} and *FF* values obtained with the $MoO_x/Al_2O_3/SiO_y$ stack imply that the interlayer presents minimal resistance to hole carriers, and likely possesses a high μ_h value of about 10^{-2} cm^2 V^{-1} s^{-1}.

To investigate the impact of μ_h on recombination losses and cell efficiency, we analysed the simulated *JV* curves and recombination current distributions. Figures 10a and 10b depict the simulated *JV* curves and recombination current densities at the *p*- and *n*-contacts, and within the absorber (bulk) for μ_h values of 10^{-5} and 10^{-7} cm^{2}V^{-1}s^{-1}, respectively, at a hole contact WF of 5.21 eV. At $\mu_h = 10^{-5}$ cm^2 V^{-1} s^{-1}, the total current (extracted current minus recombination current) follows a diode-like behaviour, resulting in a high *FF*. Here, recombination within the bulk absorber is the primary efficiency-limiting factor. However, when μ_h is reduced to 10^{-7} cm^2 V^{-1} s^{-1}, the *FF* decreases significantly, and the *JV* curve exhibits an S-shape. This indicates that while bulk recombination remains dominant, it no longer follows a simple diode behaviour. The high R_h at the low-mobility interlayer impedes hole transport, forcing the majority hole carriers holes to recombine within the c-Si bulk, as shown by the J_r in Figure 10b.

4 Discussion

While the mobility model employed in this study simplifies carrier transport across the MoO_x contacts, it is essential to acknowledge the complexity of the actual contacts. In reality, several transport mechanisms, such as thermionic emission, band-to-band tunneling, and trap-assisted tunneling, exist at the interfaces of the MoO_x contacts. Additionally, the influence of the TCO layer and interlayer formation at the interfaces were not considered in this model, potentially introducing additional transport limitations. Nevertheless, as a comparative study, the presented model proves valuable in discerning differences in observed selectivity losses and recognizing the limitations imposed by the interlayers on the MoO_x contacts. The following section explains the differences in contact selectivity of the MoO_x contacts.

The combination of an a-Si:H(i) interlayer with MoO_x contact shows excellent surface passivation properties, but results in a decreasing hole selectivity with increasing annealing temperature compared to an Al_2O_3/SiO_y interlayer. Several factors can contribute to this difference: (1) the degradation of induced band bending with annealing temperature which is also exacerbated by the presence of an a-Si:H(i) interlayer – possibly attributed to a pronounced Fermi level pinning effect [38,39]; (2) high contact resistance resulting from an intermixed oxide region formed at the interface between the MoO_x and a-Si:H(i) interlayer, combined with the sensitive alignment between the MoO_x conduction band and valence band of the a-Si:H(i) interlayer [40,41]. The latter arises from the necessity of closely aligning the conduction band of the MoO_x layer with the valence band of the a-Si:H(i) layer for efficient tunneling transport.

By omitting the a-Si:H(i) interlayer, good contact selectivity and *FF* were obtained but the MoO_x/c-Si contact lacks surface passivation properties. The surface passivation and carrier selectivity of the MoO_x contact improve by inserting an ultrathin Al_2O_3/SiO_y stack, resulting in higher *FF* and V_{oc} values, low E_a, and improved contact thermal stability. This improvement can be attributed to the high hole mobility of approximately 10^{-2} cm^2 V^{-1} s^{-1} of the Al_2O_3/SiO_y interlayer, which does not impede the extraction of majority hole charge carriers. This effect is linked to the amorphous and non-stoichiometric nature of the ultrathin

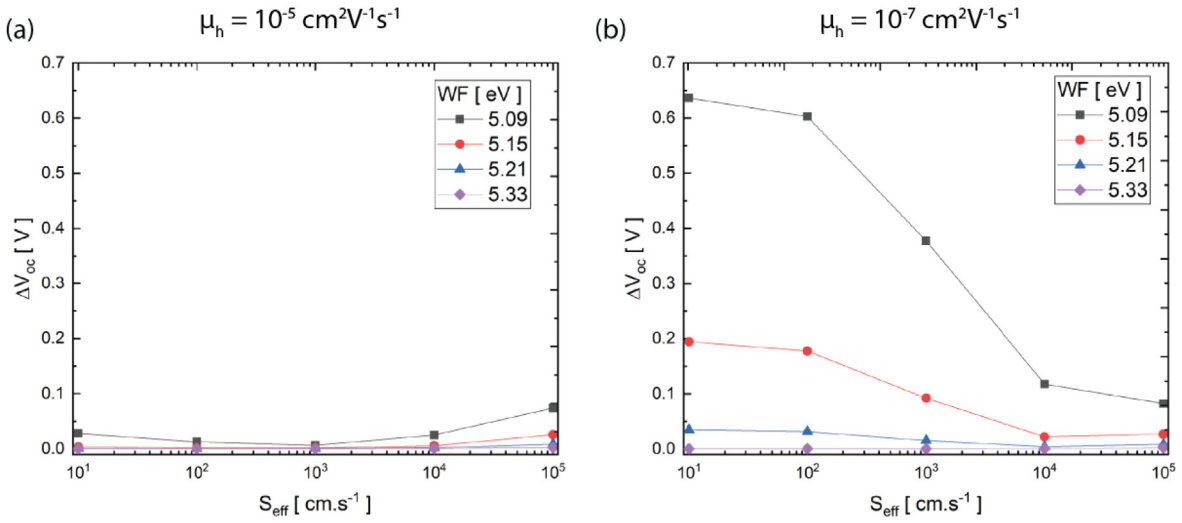

Fig. 8. Simulated ΔV_{oc} as a function of S_{eff} for the hole contact shown for WF varying from 5.09 to 5.33 eV and for μ_h of (a) 10^{-5} $cm^2V^{-1}s^{-1}$ and (b) 10^{-7} $cm^2V^{-1}s^{-1}$.

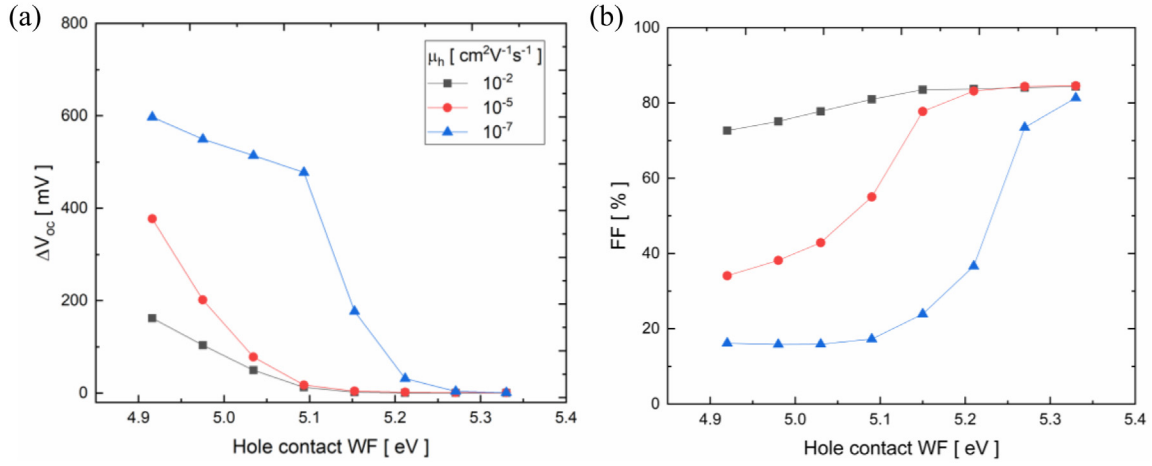

Fig. 9. Simulated effect of varying μ_h (10^{-2}–$10^{-7}$$cm^2V^{-1}s^{-1}$) and hole *WF* contact (4.92–5.34 eV) (a) on ΔV_{oc}, (b) and on *FF*. S_{eff} is set to 33 cm/s which is representative of the surface passivation quality of Al_2O_3/SiO_y and SiO_2 interlayers with a MoO_x contact. Electron mobility of the interlayer is set to 10^{-5} $cm^2V^{-1}s^{-1}$.

SiO_y layer formed at the c-Si surface, as shown in [21]. Furthermore, the considerably low E_a suggests a smaller valence band offset (VBO) between SiO_y and c-Si, thereby facilitating the transport of holes. While both thermionic emission and tunneling can contribute to carrier transport through thin oxide layers, the low E_a value for the $MoO_x/Al_2O_3/SiO_y$ contact is consistent with typical thermionic emission barriers reported for similar structures [42,43]. Similarly, several studies show that oxygen incorporation in a-SiO_x:H interlayers result in an inefficient hole transport and consequently in an S-shaped *IV* curve [4,44]. In addition, Al_2O_3/SiO_y films on c-Si substrates typically consist of high negative fixed charge properties which can promote the collection of holes as majority carriers; an inversion layer near the c-Si surface is created which increases the hole concentration. The negative fixed charged of our Al_2O_3/SiO_y film was, indeed, detected by conducting a corona charge experiment. However, further work is required to quantify the magnitude of this fixed charge of the layer due to the quick dissipation of charges after corona charge deposition. Further details can be found in Appendix B.

In comparison, a high carrier selectivity loss is apparent for the thermally grown SiO_2 interlayer although surface passivation properties similar to the Al_2O_3/SiO_y interlayer were achieved; surface passivation affects the hole resistance near the c-Si surface which ultimately influences the hole selectivity [25,37]. Additionally, the large disparity in the calculated E_a between the two interlayers suggests differences in transport mechanisms. The high E_a for SiO_2 indicates a larger energy barrier, likely hindering thermionic emission and suggesting that tunneling is the dominant transport mechanism, which is less efficient than thermionic emission. This is in contrast to the Al_2O_3/SiO_y interlayer, where the low E_a suggests a smaller barrier

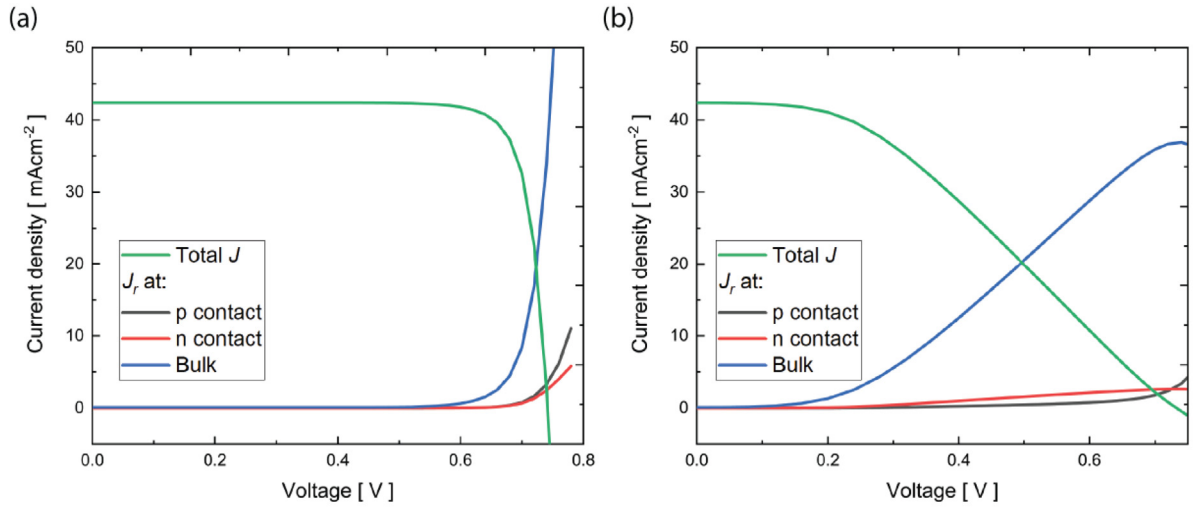

Fig. 10. Simulated JV curves, and recombination currents at the p- and n- contact, and in the absorber (bulk) as a function of cell voltage, for μ_h of (a) 10^{-5} and (b) 10^{-7} cm^{2}V^{-1}s^{-1}.

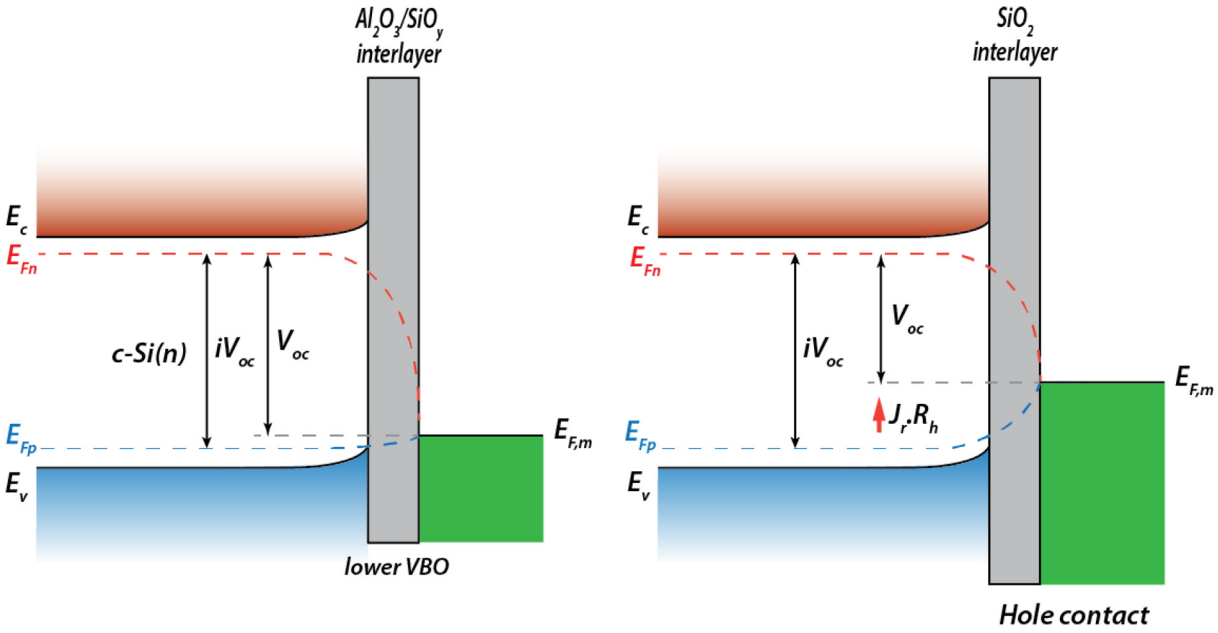

Fig. 11. Schematic band diagrams of hole contacts with Al_2O_3/SiO_y (left) and SiO_2 (right) interlayers, illustrating the contrasting energy barriers and hole and electron quasi-Fermi levels ($E_{Fp,n}$) alignment.

resulting in a more effective thermionic emission. The observed ΔV_{oc} and FF losses of the MoO_x/SiO_2/c-Si contact are likely the result of a significantly lower interlayer μ_h in the range of 10^{-7} to 10^{-8} cm^2 V^{-1} s^{-1}. This difference in layer mobility is likely caused by a large VBO with c-Si (4.7 eV) of the SiO_2 interlayer which creates a large barrier for holes. As a result, a significant step in the quasi-Fermi level of the holes (E_{Fp}) is introduced at the interface, as illustrated in Figure 11, thereby reducing the current towards the hole contact. This step acts as an additional barrier to hole extraction, further impeding the flow of holes through the contact resulting in an increase in $J_{r,abs}$. This increases $R_{h,int}$ which consequently contributes to the observed loss in carrier selectivity.

Although the contact selectivity loss can be reduced by increasing the contact WF, such high contact WF is often not feasible. In practice, a more effective approach is to enhance the interlayer mobility. For instance, in the case of poly-Si(p^+) contacts, a post-deposition annealing step at high temperature is usually required for boron diffusion from the poly-Si to the SiO_2 and c-Si absorber. The increase in boron concentration in the poly-Si(p^+) increases the contact WF, but also causes an increase in boron diffusion inside the Si substrate, leading to a higher defect density at the interface. Nevertheless, this post-deposition annealing

step is crucial in enhancing the hole mobility across the SiO_2 interlayer; this process allows for the creation of pinholes and/or to reduce the interlayer thickness, thereby improving the transport of holes [45]. For MoO_x/SiO_2 contacts, a high temperature treatment is not viable due to the lack of thermal stability of the MoO_x layer [46].

Additionally, the thermal instability of the MoO_x contact poses challenges in implementing post-hydrogenation techniques to enhance the surface passivation at the Si/interlayer interface. Conventionally, the diffusion of hydrogen to the interface of poly-Si contacts can be achieved in several different schemes such as hydrogen-rich capping layers or a remote hydrogen plasma treatment [47,48]. However, in the case of MoO_x contacts, similar hydrogenation techniques are challenging since the MoO_x layer interacts with hydrogen thereby degrading the *WF* value of the MoO_x layer [49]. The introduction of an ALD Al_2O_3 interlayer addresses some of these issues, allowing for improvement of the surface passivation without compromising on the contact selectivity. While further layer optimizations and post-deposition treatments on the Al_2O_3 interlayer can be developed to enhance the surface passivation properties, it must be ensured that these processes do not compromise the interlayer hole mobility, keeping it above 10^{-5} cm^2 V^{-1} s^{-1}.

5 Conclusion

In this work, we highlight the importance of high hole contact *WF* to create a strong induced band bending near the c-Si interface and the necessity of a sufficient hole mobility through the interlayer to achieve an effective hole-selective contact. An a-Si:H(i) interlayer can provide excellent surface passivation, but the MoO_x *WF* loss upon a thermal annealing treatment results in observable contact selectivity loss. On the other hand, a dense, stoichiometric, thermally grown SiO_2 interlayer will cause considerable contact selectivity losses if no post-treatment is performed to improve the hole mobility. An ultrathin Al_2O_3/SiO_y interlayer provides better transparency, hole transport, and thermal stability when combined with MoO_x. This is because the sub-stoichiometric SiO_y layer does not hinder the transport of holes across the Al_2O_3/SiO_y interlayer. Hydrogenation strategies prior to the MoO_x deposition can be explored to improve the surface passivation provided by the Al_2O_3/SiO_y interlayer stack to ultimately improve the quality of MoO_x-based contacts in c-Si solar cells.

Funding

The authors would like to thank Martien Koppes, Eelko Hoek, and Benjamin Kikkert for the fabrication of the solar cells. This work was financially supported by Top consortia for Knowledge and Innovation (TKI) Solar Energy programs "COMPASS" (TEID215022), "RADAR" (TEUE116905) and MOMENTUM (TKI Energy PPS Toeslag project number: 1821101) of the Ministry of Economic Affairs of The Netherlands.

Conflicts of interest

The authors have no conflicts to disclose.

Data availability statement

The data that support the findings of this study are available from the corresponding author upon reasonable request.

Author contribution statement

Conceptualization, M.T.S.K. Ah Sen, P. Bronsveld, and G. Janssen.; Methodology, M.T.S.K. Ah Sen and G. Janssen.; Software, M.T.S.K. Ah Sen and G. Janssen.; Validation, M.T.S.K. Ah Sen and G. Janssen.; Formal Analysis, M.T.S.K. Ah Sen and G. Janssen.; Investigation, M.T.S.K. Ah Sen.; Resources, M.T.S.K. Ah Sen, P. Bronsveld, and A. Weeber; Data Curation, M.T.S.K. Ah Sen; Writing – Original Draft Preparation, M.T.S.K. Ah Sen.; Writing – Review & Editing, M.T.S.K. Ah Sen, G. Janssen, A. Mewe, P. Bronsveld, J. Melskens, F. Hashemi, P. Procel, and A. Weeber; Visualization, M.T.S.K. Ah Sen; Supervision, P. Bronsveld, J. Melskens, and A. Weeber; Project Administration, P. Bronsveld and A. Weeber; Funding Acquisition, P. Bronsveld, J. Melskens.

Appendix: A

We investigate the impact of x-ray-induced surface passivation damage, occurring during MoO_x deposition, on the surface passivating properties of the interlayers. 6 nm thick AlO_x layers were deposited on both sides of a c-Si(n) substrate, followed by post-deposition annealing (PDA) at 600 °C. To assess the effect of X-ray induced damage from MoO_x e-beam deposition, a glass sheet is placed on top of the AlO_x passivated sample, preventing MoOx deposition while allowing x-ray emission to pass through. Figure A.1 shows the effective lifetime (τ_{eff}) measured at a carrier concentration of 10^{15} cm^{-3} for both a reference sample and a sample subjected to the x-rays. AlOx samples with X-ray induced damage show similar τ_{eff} as the AlO_x reference sample. The negligible difference between the samples implies that the induced X-ray damage has minimal effect on the surface passivating quality. This is possibly because of the low e-beam power used during the MoO_x deposition; MoO_x has a low sublimation point and therefore only requires little energy to evaporate.

Appendix: B

To assess the impact of the passivating interlayers on the induced band bending, we use a corona charging setup by Delft Spectral Technologies for samples shown in Figure B.1. Further details about the corona charging tool can be found in references [49–53]. The samples with

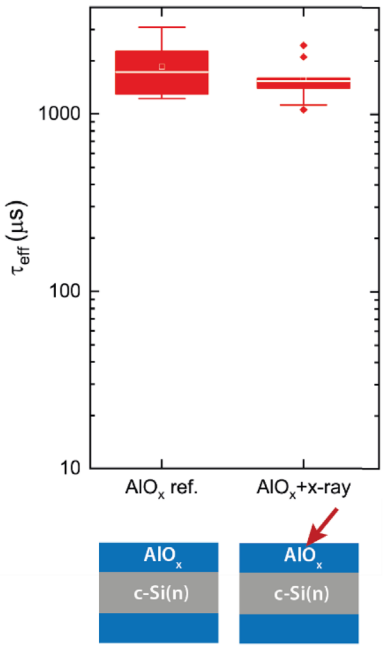

Fig. A.1. Comparing the surface passivation quality between passivated AlO_x reference and x-ray exposed samples.

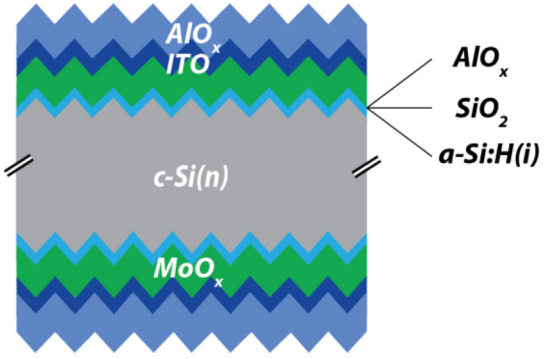

Fig. B.1. Symmetric samples consisting of AlO_x, SiO_2, and a-Si:H(i) interlayers, capped with MoO_x, ITO, and AlO_x.

AlO_x, SiO_2, and a-Si:H(i) interlayers were capped with MoO_x, a thin layer of indium tin oxide (ITO), and 6 nm of AlO_x to reduce the dissipation of charges. To ensure of more representative stack, a thin ITO layer was added and further capped with AlO_x to minimize the potential charge dissipation.

Note here that $S_{eff,max}$ was calculated from the wafer thickness W and the effective minority carrier lifetime τ_{eff} ($S_{eff,max} = W / 2\tau_{eff}$) after conducting quasi-steady state photoconductance (QSSPC) measurements using a Sinton WCT-120TS setup in the generalized (1/64) mode. For the QSSPC measurements we assumed n-type substrates, a wafer thickness of 200 µm, an optical constant of 0.55 (for chemically polished substrates) and the τ_{eff} values at an injection level of $1 \cdot 10^{15}$ cm^{-3} were used for the calculation of $S_{eff,max}$.

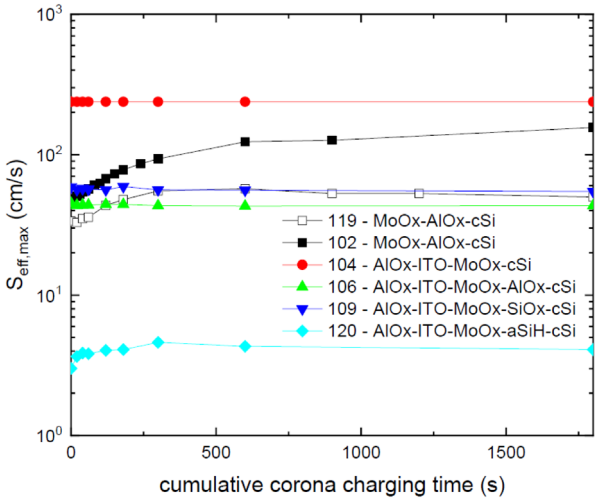

Fig. B.2. S_{eff} against cumulative charge deposition time for MoO_x samples.

We have conducted positive charging on both sides of all samples in an attempt to derive the fixed charge density (Qf). Figure B.2 shows the effect of the cumulative induced positive charges on the S_{eff} values of the samples. However, the fixed charge density could not be reliably determined for these samples due to a minimal change in passivation quality after charge deposition combined with leaky behavior. As a result, no increase in $S_{eff,max}$ is observed with increasing cumulative corona charging time. For samples with ITO, no significant changes in $S_{eff,max}$ are observed throughout the experiment, which can be understood as mirror charges that appear in the top part of the ITO layer upon corona charge deposition such that the silicon surface is effectively shielded to the point that no change in the field effect passivation can be realized. For samples without ITO, a more pronounced degradation of S_{eff} can be observed by which the $S_{eff,max}$ is determined after 600 s. Nevertheless, the amplitude of the curve is rather small resulting in a high uncertainty.

To estimate the amount of deposited corona charge up until the maximum in $S_{eff,max}$ is reached, the increase in the Kelvin probe voltage VKP over time is linearly fitted, as is shown in Figure B.3. Although the resulting fit does not clearly follow a linear trend, this kind of approximation is anyway used to estimate the change in V_{KP} that is required for the evaluation of fixed charged density (Q_f). The poor quality of the linear fit further illustrates that the error on the Q_f value that will be calculated below should only be taken as a lower limit. Furthermore, it is interesting how the slope of the fitted line corresponds to the approximate slope corresponding to the samples with ITO/AlO_x capping, while beyond 600 s the uncapped MoO_x layer is not able to retain any additional charge due to leaky behavior. Following the plotted fitting approach, the total amount of deposited corona charge is estimated from the difference in V_{KP} between the value at the start of the experiment and the value after 600 s of charging using the slope of the fitted line: $\Delta V_{KP} = 7.075 \cdot 10^{-4} * 600 = 0.424$ V. Note here that 600 s is the point in the experiment where

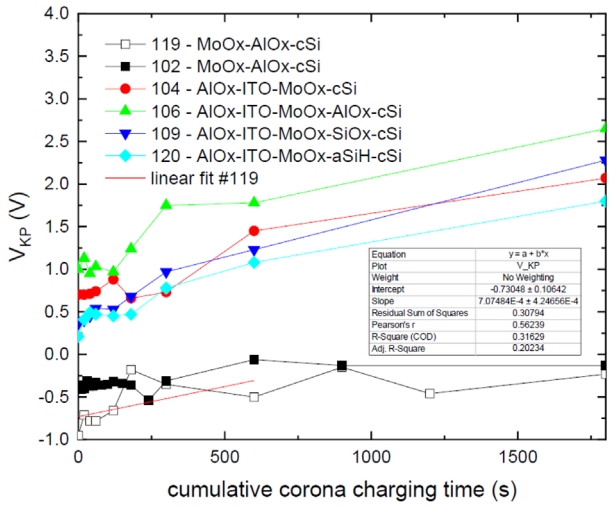

Fig. B.3. V_{KP} as a function of cumulative corona charging time for MoO_x contacts with different interlayers.

the maximum in $S_{eff,max}$ is reached that can in turn be used to calculate Q_f, as follows:

$$Q_{corona} = \frac{\varepsilon_r \varepsilon_0}{d} \cdot \frac{V_{KP}}{e} \quad \text{(A1)}$$

where ε_0 is the vacuum permittivity (8.854×10^{-12} Fm^{-1}), ε_r is the relative permittivity of MoO_x (18), d is the thickness of the layer stack (5 nm), and e is the elementary charge. Since the deposited corona charge counteracts the fixed charge that is initially present in the layer stack, it holds that $Q_f = -2.0 \pm 1.0 \times 10^{12}$ cm^{-2}. This moderately negative fixed charge could be associated with traps in the MoO_x layer that are being filled in the corona charging experiment. If this is correct, other variations in the MoO_x layer properties, such as what is induced by different growth temperatures, and their possible impact on Q_f could become detectable by further corona charging experiments.

References

1. H. Lin, M. Yang, X. Ru, G. Wang, S. Yin, F. Peng, C. Hong, M. Qu, J. Lu, L. Fang, C. Han, P. Porcel, O. Isabella, P. Gao, Z. Li, X. Xu, Silicon heterojunction solar cells with up to 26.81% efficiency achieved by electrically optimized nanocrystalline-silicon hole contact layers, Nat. Energy **8**, 789 (2023)
2. JinkoSolar Holding Co., Ltd, JinkoSolar's High-efficiency N-Type Monocrystalline Silicon Solar Cell Sets New Record with Maximum Conversion Efficiency of 26.89% [Press release]. Available at https://www.prnewswire.com/news-releases/jinkosolars-high-efficiency-n-type-monocrystalline-silicon-solar-cell-sets-new-record-with-maximum-conversion-efficiency-of-26-89- 3019 71256.html (access: 13.02.2024)
3. A. Richter, R. Müller, J. Benick, F. Feldmann, B. Steinhauser, C. Reichel, A. Fell, M. Bivour, M. Hermle, S.W. Glunz, Design rules for high-efficiency both-sides-contacted silicon solar cells with balanced charge carrier transport and recombination losses, Nat. Energy **6**, 429 (2021)
4. J. Peter Seif, A. Descoeudres, M. Filipič, F. Smole, M. Topič, Z. Charles Holman, S. De Wolf, C. Ballif, Amorphous silicon oxide window layers for high-efficiency silicon heterojunction solar cells, J. Appl. Phys. **115**, 024502 (2014)
5. Z.C .Holman, A. Descoeudres, L. Barraud, F.Z. Fernandez, J.P. Seif, S. De Wolf, C. Ballif, Current losses at the front of silicon heterojunction solar cells, IEEE J. Photovolt. **2**, 7 (2012)
6. J. Melskens, B.W.H. Van De Loo, B. Macco, L.E. Black, S. Smit, W.M.M. Kessels, Passivating contacts for crystalline silicon solar cells: from concepts and materials to prospects, IEEE J. Photovolt. **8**, 373 (2018)
7. L.E. Black, B.W.H. van de Loo, B. Macco, J. Melskens, W.J. H. Berghuis, W.M.M. Kessels, Explorative studies of novel silicon surface passivation materials: considerations and lessons learned, Sol. Energy Mater. Sol. Cells **188**, 182 (2018)
8. C. Battaglia, X. Yin, M. Zheng, I.D. Sharp, T. Chen, S. Mcdonnell, A. Azcatl, C. Carraro, B. Ma, R. Maboudian, R. M. Wallace, A. Javey, Hole selective MoOx contact for silicon solar cells, Nano Lett. **14**, 967 (2014)
9. C. Battaglia, S.M. De Nicolás, S. De Wolf, X. Yin, M. Zheng, C. Ballif, A. Javey, Silicon heterojunction solar cell with passivated hole selective MoOx contact, Appl. Phys. Lett. **104**, 1 (2014)
10. J. Bullock, D. Yan, A. Cuevas, Y. Wan, C. Samundsett, *n*- and *p*-typesilicon solar cells with molybdenum oxide hole contacts, Energy Proc. **77**, 446 (2015)
11. J. Bullock, M. Hettick, J. Geissbühler, A.J. Ong, T. Allen, C.M. Sutter-Fella, T. Chen, H. Ota, E.W. Schaler, S. De Wolf, C. Ballif, A. Cuevas, A. Javey, Efficient silicon solar cells with dopant-free asymmetric heterocontacts, Nat. Energy **1**, 1 (2016)
12. L. Cao, P. Procel, A. Alcañiz, J. Yan, F. Tichelaar, E. Özkol, Y. Zhao, C. Han, G. Yang, Z. Yao, M. Zeman, R. Santbergen, L. Mazzarella, O. Isabella, Achieving 23.83% conversion efficiency in silicon heterojunction solar cell with ultra-thin MoOx hole collector layer via tailoring (i) a-Si:H/MoOx interface, Prog. Photovolt.: Res. Appl. **31**, 1245 (2022)
13. J. Geissbühler, J. Werner, S. Martin De Nicolas, L. Barraud, A. Hessler-Wyser, M. Despeisse, S. Nicolay, A. Tomasi, B. Niesen, S. De Wolf, C. Ballif, 22.5% efficient silicon heterojunction solar cell with molybdenum oxide hole collector, Appl. Phys. Lett. **107**, 081601 (2015)
14. L. Neusel, M. Bivour, M. Hermle, Selectivity issues of MoOx-based hole contacts, Energy Proc. **124**, 425 (2017)
15. S.W. Glunz, F. Feldmann, A. Richter, M. Bivour, C. Reichel, H. Steinkemper, J. Benick, M. Hermle, The irresistible charm of a simple current flow pattern-25% with a solar cell featuring a full-area back contact, in *Proceedings of the 31st European Photovoltaic Solar Energy Conference and Exhibition* (München, Germany, 2015), p. 259
16. M. Boccard, X. Yang, K. Weber, Z.C. Holman, Passivation and carrier selectivity of TiO2 contacts combined with different passivation layers and electrodes for silicon solar cells, in *Conference Record of the IEEE Photovoltaic Specialists Conference* (2016), pp. 2403–2407
17. T. Kamioka, Y. Hayashi, Y. Isogai, K. Nakamura, Y. Ohshita, Effects of annealing temperature on workfunction of MoOx at MoOx/SiO2 interface and process-induced damage in indium tin oxide/MoOx/SiOx/Si stack, Jpn. J. Appl. Phys. **57**, 076501 (2018)

18. J. Tong, T.T. Le, W. Liang, M.A. Hossain, K.R. McIntosh, P. Narangari, S. Armand, T.C. Kho, K.T. Khoo, Y. Zakaria, A.A. Abdallah, S. Surve, M. Ernst, B. Hoex, K.C. Fong, Impact of pregrown SiOx on the carrier selectivity and thermal stability of molybdenum-oxide-passivated contact for Si solar cells, ACS Appl. Mater. Interfaces **13**, 36426 (2021)
19. M. Bivour, B. Macco, J. Temmler, W.M.M. Kessels, M. Hermle, Atomic layer deposited molybdenum oxide for the hole-selective contact of silicon solar cells, Energy Proc. **92**, 443 (2016)
20. B.E. Davis, N.C. Strandwitz, Aluminum oxide passivating tunneling interlayers for molybdenum oxide hole-selective contacts, IEEE J. Photovolt. **10**, 722 (2020)
21. M.T.S.K. Ah Sen, P. Bronsveld, A. Weeber, Thermally stable MoOx hole selective contact with Al2O3 interlayer for industrial size silicon solar cells, Sol. Energy Mater. Sol. Cells **230**, 111139 (2021)
22. V. Naumann, M. Otto, R.B. Wehrspohn, C. Hagendorf, Chemical and structural study of electrically passivating Al2O3/Si interfaces prepared by atomic layer deposition, J. Vacuum Sci. Technol. A **30**, 04D106 (2012)
23. O. Renault, L.G. Gosset, D. Rouchon, A. Ermolieff, Angle-resolved x-ray photoelectron spectroscopy of ultrathin Al2O3 films grown by atomic layer deposition, J. Vac. Sci. Technol. A **20**, 1867 (2002)
24. A. Sarkar, *Device simulation using Silvaco ATLAS tool*, *Technology Computer Aided Design* (CRC Press, Boca Raton, Florida, USA, 2018), p. 203252
25. G.J.M. Janssen, M.T.S.K. Ah Sen, P.C.P. Bronsveld, A simplified model to simulate passivating & selective hole-collecting contacts, in *Proceeding 36th European Photovoltaic Solar Energy Conference and Exhibition* (Marseille, France, 2019), pp. 2–8
26. U. Wurfel, A. Cuevas, P. Wurfel, Charge carrier separation in solar cells, IEEE J. Photovolt. **5**, 461 (2015)
27. G. Janssen, M. Stodolny, I. Romijn, B. Geerligs, The role of the oxide in the carrier selectivity of metal/poly-Si/oxide contacts to silicon wafers, in *Proceeding 33rd European Photovoltaic Solar Energy Conference and Exhibition* (Amsterdam, The Netherlands, 2017), pp. 256–261
28. F. Feldmann, G. Nogay, J.I. Polzin, B. Steinhauser, A. Richter, A. Fell, C. Schmiga, M. Hermle, S.W. Glunz, A study on the charge carrier transport of passivating contacts, IEEE J. Photovolt. **8**, 1503 (2018)
29. D.B.M. Klaassen, A unified mobility model for device simulation—I. Model equations and concentration dependence, Solid-State Electron. **35**, 953 (1992)
30. A. Richter, S. Glunz, F. Werner, J. Schmidt, Improved quantitative description of Auger recombination in crystalline silicon, Phys. Rev. B **86**, 165202 (2012)
31. L.G. Gerling, C. Voz, R. Alcubilla, J. Puigdollers, Origin of passivation in hole-selective transition metal oxides for crystalline silicon heterojunction solar cells, J. Mater. Res. **32**, 260 (2017)
32. B.B. Demaurex, S. De Wolf, A. Descoeudres, Z. Charles Holman, C. Ballif, Damage at hydrogenated amorphous/crystalline silicon interfaces by indium tin oxide overlayer sputtering, Appl. Phys. Lett. **101**, 171604 (2012)
33. M.T.S.K. Ah Sen, A. Mewe, J. Melskens, J. Bolding, M. Van de Poll, A. Weeber, Soft deposition of TCOs by pulsed laser for high-quality ultra-thin poly-Si passivating contacts, J. Appl. Phys. **134**, 154502 (2023)
34. M. Bivour, C. Messmer, L. Neusel, F. Zähringer, J. Schön, S. W. Glunz, M. Hermle, Principles of carrier-selective contacts based on induced junctions, in *Proceeding 33rd European PV Solar Energy Conference and Exhibition* (Amsterdam, The Netherlands, 2017), pp. 25–29
35. S. Essig, J. Dréon, E. Rucavado, M. Mews, T. Koida, M. Boccard, J. Werner, J. Geissbühler, P. Löper, M. Morales-Masis, L. Korte, S. De Wolf, C. Balllif, Toward annealing-stable molybdenum-oxide-based hole-selective contacts for silicon photovoltaics, Solar RRL **2**, 1700227 (2018)
36. J.P. Seif, D. Menda, A. Descoeudres, L. Barraud, O. Özdemir, C. Ballif, , S. De Wolf, Asymmetric band offsets in silicon heterojunction solar cells: Impact on device performance, J. Appl. Phys. **120**, 054501 (2016)
37. A. Onno, C. Chen, Z.C. Holman, Electron and hole partial specific resistances: A framework to understand contacts to solar cells, in *Conference Record of the IEEE Photovoltaic Specialists Conference* (2019), pp. 2329–2333
38. D. Sacchetto, Q. Jeangros, G. Christmann, L. Barraud, A. Descoeudres, J. Geissbuhler, M. Despeisse, A. Hessler-Wyser, S. Nicolay, C. Ballif, ITO/MoOx/a-Si:H(i) hole-selective contacts for silicon heterojunction solar cells: degradation mechanisms and cell integration, IEEE J. Photovolt. **7**, 1584 (2017)
39. J. Cho, N. Nawal, A. Hadipour, M. Recaman Payo, A. van der Heide, H.S. Radhakrishnan, M. Debucquoy, I. Gordon, J. Szlufcik, J. Poortmans, Interface analysis and intrinsic thermal stability of MoOx based hole-selective contacts for silicon heterojunction solar cells, Sol. Energy Mater. Sol. Cells **201**, 110074 (2019)
40. C. Messmer, M. Bivour, J. Schön, S.W. Glunz, M. Hermle, J. Schon, S.W. Glunz, M. Hermle, Numerical simulation of silicon heterojunction solar cells featuring metal oxides as carrier-selective contacts, IEEE J. Photovolt. **8**, 456 (2018)
41. S.M. Sze, K.K. Ng, *Physics of Semiconductor Devices*, 3rd edn. (Wiley-Interscience, 2006)
42. R.T. Tung, Recent advances in Schottky barrier concepts, Mater. Sci. Eng. R Rep. **35**, 1 (2001)
43. M. Liebhaber, M. Mews, L. Korte, T.F. Schulze, B. Rech, K. Lips, Valence band offset and hole transport across a-SiOx ($0<x<2$) passivation layers in silicon heterojunction solar cells, in *31st European Photovoltaic Solar Energy Conference and Exhibition (i),* (2015) pp. 770–775
44. J. Bullock, A. Cuevas, T. Allen, C. Battaglia, Molybdenum oxide MoOx: a versatile hole contact for silicon solar cells, Appl. Phys. Lett. **105**, 232109 (2014)
45. R. Peibst, U. Römer, Y. Larionova, M. Rienäcker, A. Merkle, N. Folchert, S. Reiter, M. Turcu, B. Min, J. Krügener, D. Tetzlaff, E. Bugiel, T. Wietler, R. Brendel, Working principle of carrier selective poly-Si/c-Si junctions: is tunnelling the whole story? Sol. Energy Mater. Sol. Cells **158**, 60 (2016)
46. J. Cho, N. Nawal, A. Hadipour, M. Recaman Payo, A. van der Heide, H.S. Radhakrishnan, M. Debucquoy, I. Gordon, J. Szlufcik, J. Poortmans, Interface analysis and intrinsic thermal stability of MoOx based hole-selective contacts for silicon heterojunction solar cells, Sol. Energy Mater. Sol. Cells **201**, 110074 (2019)
47. B.W.H. van de Loo, B. Macco, M. Schnabel, M.K. Stodolny, A.A. Mewe, D.L. Young, W. Nemeth, P. Stradins, W.M.M. Kessels, On the hydrogenation of Poly-Si passivating contacts by Al2O3 and SiNx thin films, Sol. Energy Mater Sol. Cells **215**, 110592 (2020)

48. F. Feldmann, M. Simon, M. Bivour, C. Reichel, M. Hermle, S.W. Glunz, Solar energy materials & solar cells efficient carrier-selective *p*- and *n*-contacts for Si solar cells, Sol. Energy Mater. Sol. Cells **131**, 100 (2014)
49. M.T.Greiner, L. Chai, M.G. Helander, W.M. Tang, Z.H. Lu, Metal/metal-oxide interfaces: How metal contacts affect the work function and band structure of MoO3, Adv. Funct. Mater. **23**, 215 (2013)
50. W.J.H. Berghuis, M. Helmes, J. Melskens, R.J. Theeuwes, W.M.M. Kessels, B. Macco, Extracting surface recombination parameters of germanium-dielectric interfaces by corona-lifetime experiments, J. Appl. Phys. **131**, 195301 (2022)
51. W.J.H. Berghuis, J. Melskens, B. Macco, R.J. Theeuwes, L.E. Black, M.A. Verheijen, W.M.M. Kessels, Excellent surface passivation of germanium by a-Si: H/Al_2O_3 stacks, J. Appl. Phys. **130**, 135303 (2021)
52. J. Melskens, R.J. Theeuwes, L.E. Black, W.J.H. Berghuis, B. Macco, P.C.P. Bronsveld, W.M.M. Kessels, Excellent passivation of *n*-type silicon surfaces enabled by pulsed-flow plasma-enhanced chemical vapor deposition of phosphorus oxide capped by aluminum oxide, Phys. Stat. Solidi **15**, 2000399 (2021)
53. W.J.H. Berghuis, J. Melskens, B. Macco, R.J. Theeuwes, M.A. Verheijen, W.M.M. Kessels, Surface passivation of germanium by atomic layer deposited Al_2O_3 nanolayers, J. Mater. Res. **36**, 571 (2021)

Cite this article as: Mike Tang Soo Kiong Ah Sen, Gaby Janssen, Agnes Mewe, Paula Bronsveld, Jimmy Melskens, Fatemeh Hashemi, Paul Procel-Moya, Arthur Weeber, Influence of passivating interlayers on the carrier selectivity of MoO_x contacts for c-Si solar cells, EPJ Photovoltaics **15**, 34 (2024)